ACS Sustainable Chemistry & Engineering

pubs.acs.org/journal/ascecg

Research Article

Ultrafine Pt_3Fe Intermetallic Electrocatalysts Formed by Ultrafast Joule Heating toward Ethanol Oxidation

Mingxing Nie, Zijian Wang, Dongxuan He, Wei Gan,* and Qunhui Yuan*

Cite This: https://doi.org/10.1021/acssuschemeng.4c06241

Read Online

ACCESS | Metrics & More | Article Recommendations | Supporting Information

ABSTRACT: Ordered intermetallic nanocrystals display great potential for fuel cells due to their distinctive electronic and structural properties. However, the traditional synthesis usually involves long-time annealing at high temperature or surfactant/reductant with antiaggregation property, leading to decreased electrocatalytic performance. Herein, an ultrafast and surfactant-free synthesis of ordered sub−5-nm Pt_3Fe nanocrystal-based electrocatalysts was reported (O−Pt_3Fe/rGO). Through Joule heating, Pt_3Fe nanocrystals were formed *in situ* on reduced graphene oxide within dozens of seconds. The modulation of the ordered or disordered structure of the Pt_3Fe alloys could also be achieved by the simple adjustment of experimental parameters. O−Pt_3Fe/rGO with a unique structure shows a superior mass activity of 5.66 A mg^{-1} toward ethanol oxidation reactions (EOR), which is 7.1 and 2.5 times higher than the values of the benchmark Pt/C and the counterpart catalysts containing disordered Pt_3Fe nanoalloys (D-Pt_3Fe/rGO). O−Pt_3Fe/rGO also demonstrates superb long-term stability, retaining ∼80.7% of its original mass activity after electrochemical aging. Density functional theory (DFT) calculations reveal that the catalysts with ordered Pt_3Fe show downshifted d-band center, weakened CO adsorption, enhanced OH adsorption, and improved C−C cleavage capability compared with the one with disordered Pt_3Fe. This study provides a new perspective for the efficient synthesis of highly ordered intermetallic compound catalysts for energy conversion.

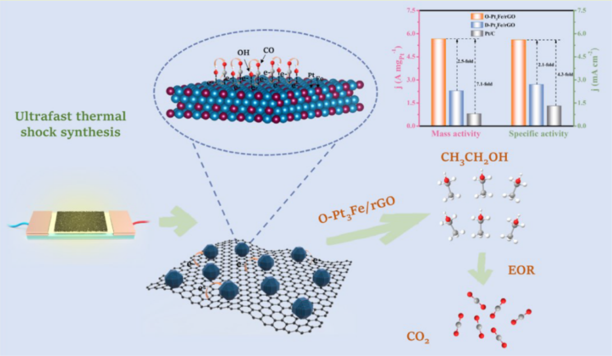

KEYWORDS: *ordered intermetallic compounds, ultrafine nanoalloys, ultrafast synthesis, Joule heating, ethanol oxidation*

1. INTRODUCTION

The consumption of carbonaceous energy and consequent environmental pollution have called for the evolution and reconstruction of energy systems.[1,2,3] In this regard, fuel cell is a promising way for its advantages of high energy conversion efficiency, low emission, wide range of fuel sources, and heavy duty affordability.[4] Among various types of fuel cells, direct ethanol fuel cell (DEFC) displays application prospect due to the merits of ethanol fuel, which shows low toxicity, high volumetric energy density, and easy accessibility.[5,6]

Nevertheless, the sluggish anodic ethanol oxidation hinders the practical applications of DEFC.[7] To improve the reaction kinetics, massive attentions have been focused on developing Pt and Pt-based catalysts, attributable to their admirable catalytic activities toward EOR.[8,9] For pure Pt catalysts, a sufficiently high Pt loading is required to achieve a satisfying catalytic activity, which makes the catalysts costly. Although small-sized Pt nanoparticles have been designed to achieve better Pt utilization, the aggregation and structural deformation of Pt nanoparticles in corrosive electrochemical media are inevitable.[10] Besides, the complete conversion from ethanol to CO_2 is challenging due to insufficient C−C cleavage ability. Additionally, the catalyst poisoning caused by CO and relevant intermediates are prone to occur.[11] These all make pure Pt catalysts less competitive. In this case, the catalyst design based on Pt and non-noble metal attracts attention.

Recently, researchers have been very interested in alloying Pt with Fe. The introduction of Fe not only reduces the cost of catalysts but also promotes EOR catalytic performance. For example, Pt/C and PtFe/C nanoparticles with small sizes ranging from 2 to 3 nm were prepared via a chemical reduction strategy and used for ethanol oxidation.[12] The synthesized PtFe/C nanoparticles exhibited a mass activity of 0.81 A mg^{-1}, which was 3.6 times that of Pt/C. Zhang et al. fabricated the networked wicker-like PtFe NWs with branch-rich exteriors on the rough surface of each nanowire.[13] The optimized Pt_3Fe NWs showed the best catalytic performance and stability among the catalysts for EOR, which were much higher than the Pt/C catalysts. A fabrication of Pt_3Fe binary nanoparticles

Received: July 29, 2024
Revised: October 18, 2024
Accepted: October 18, 2024

anchored on XC-72R support (Pt_3Fe/C) was also reported, which was achieved through a simple impregnation-reduction route coupled with high-temperature annealing.[14] Pt_3Fe/C catalysts delivered a higher catalytic activity and stability for EOR compared with Pt/C because it enabled the oxidation of CO-like intermediates at lower potentials. In general, the doped Fe modulates the electronic structure of Pt catalysts via the electronic effect and ligand effect, which would alleviate the Pt poisoning caused by CO intermediates.[15,16] According to the bifunctional mechanism, Fe promoters provide additional hydroxyl radicals to the neighboring Pt atoms and accelerate the removal of CO or other intermediates that are ready to be oxidized.[17] To achieve better catalytic performance, the development of structurally ordered PtFe intermetallic compound catalysts is a plausible route.[18,19] Compared with disordered PtFe nanoalloys, the ordered intermetallic compounds possess more excellent chemical and structural stability due to their unique electronic and geometric structures on atomic scales.[20,21−24]

In the meantime, it is still challenging to synthesize Pt-based intermetallic compounds with ultrafine sizes ($\leq$5 nm) due to rigorous empirical conditions and difficulty in controlling the ordered structures. To facilitate the migration and fusion of metallic atoms, high-temperature annealing lasting for hours is generally required, which often causes the sintering of particles with uneven particle size.[25] The wet chemical strategy can fulfill the synthesis at lower temperature. However, surface stabilizers are often required to restrict the growth of the nanoparticles, which block the active sites and result in obstructive catalytic performance of catalysts.[26,27] In these regards, syntheses through strategies with mild conditions or short times such as microwave radiation, sonochemical treatment, and electrochemical deposition have been exploited.[25] Nevertheless, strategies capable of developing Pt-based intermetallic compounds under mild conditions are still underdeveloped. Therefore, new efficient strategies are highly desirable.

Recently, a carbothermal shockwave process induced by Joule heating has been proposed for the synthesis of intermetallic compound nanoparticles owing to its rapid heating/cooling capability and elevated temperatures. For instance, Cui et al. reported the successful synthesis of multiprincipal element intermetallics (MPEIs, PtPdAuFeCoNiCuSn) through a disorder-to-order phase transition driven by Joule heating.[28] Such MPEI nanoparticles cannot be easily obtained via traditional approaches. They also synthesized highly ordered Pd_3Pb nanoparticles (~6 nm) with ultrahigh oxygen reduction reaction (ORR) stability through a similar Joule heating strategy.[29] DFT results indicated that the fast atomic ordering transformation stems from the vacancy diffusion mechanism. Yan et al. prepared $L1_2$-Pt_3Mn and $L1_0$-PtMn intermetallics with Pt skin via a periodic carbothermal shock strategy.[30] $L1_2$-Pt_3Mn exhibits better ORR catalytic activity than $L1_0$-PtMn. However, based on our current knowledge, the synthesis of intermetallic compounds through Joule heating is still in its initial phase and demands more exploration. Furthermore, there is limited study on the influence of the orderliness of Pt-based alloys on electrocatalytic performance for EOR.

It has been proven that the intermetallic compounds can enhance the oxidation of small molecules. For example, Li et al. fabricated a ternary $L1_0$-CoPtAu nanoparticle catalyst and used it in the catalytic oxidation of ethanol, methanol, and formic acid.[31] They found that such a catalyst with ternary intermetallic compounds can effectively enhance the cleavage of C−C/C−H bond. Feng et al. developed an amorphous/intermetallic PtPbBi nanosheet.[32] DFT calculations demonstrate that the preparation of multimetallic catalysts with an amorphous/intermetallic heterointerface facilitates the electron transfer from the catalysts to vital intermediates, thus enhancing the catalytic performance of the methanol oxidation reaction (MOR). Despite the abovementioned progress, the effect of ordered and disordered structures of Pt-based intermetallics on the cleavage of C−C bond in ethanol is still rare. Consequently, the synthesis and functionality of Pt-based intermetallics on EOR catalysis are worth further exploration.

In this study, a surfactant-free fabrication of structurally ordered Pt_3Fe intermetallic nanoparticles embedded in reduced graphene oxide (O−Pt_3Fe/rGO) toward EOR was reported. Through an ultrafast Joule heating strategy within a time scale of tens of seconds, the generation of rGO-supported Pt_3Fe nanoparticles at high density and high dispersity is accomplished, with an ultrafine average particle size of ~3.7 nm. By adjustment of the times of the thermal shock, the structural transformation of disordered Pt_3Fe into ordered Pt_3Fe was achieved within several tens of seconds. In this case, the effect of crystal structure of Pt-based intermetallics on the catalytic performance toward EOR could be investigated. Owing to the unique structure, O−Pt_3Fe/rGO displays a much better mass activity and stability than the commercial Pt/C and structurally disordered Pt_3Fe counterpart (D-Pt_3Fe/rGO). DFT calculation reveals that ordered Pt_3Fe possesses downshifted d-band center of Pt, weakened CO adsorption, and enhanced OH affinity facilitated C−C bond cleavage compared with disordered Pt_3Fe.

2. EXPERIMENTAL SECTION

2.1. Preparation of Pt_3Fe/GO Aerogel Precursor. The details of chemicals, structural characterizations, and DFT calculations are shown in Supporting Information (S1−S3). For the preparation of Pt_3Fe/GO aerogel precursor, 64 mg of graphene oxide (GO) was dispersed in 4 mL of water by ultrasonication for 30 min, followed by the addition of 580 μL of $[PtCl_6]^{2-}$−containing solution and 195 μL of Fe^{2+}−containing solution at 0.1 M (made from $H_2PtCl_6\cdot 6H_2O$ and $Fe(CH_3COO)_2$, respectively). The mixture was then thoroughly stirred and freeze-dried for 36 h to get the hydrogel precursor, where the atomic ratio of Pt and Fe is ~3:1.

2.2. Synthesis of D-Pt_3Fe/rGO and O−Pt_3Fe/rGO. The structurally disordered and ordered Pt_3Fe embedded in rGO were fabricated through a Joule heating treatment in an argon-filled glovebox. Briefly, the Pt_3Fe/GO aerogel precursors were ground into a powder and loaded on a conductive carbon cloth, which was connected to an external DC power supply via two copper foils. The DC power supply offered adjustable current and voltage. The corresponding temperature was recorded with an infrared thermometer. By applying a current of 12−16 A, a voltage of 32 V, and a one-time heating treatment of 2 s, D-Pt_3Fe/rGO was synthesized. O−Pt_3Fe/rGO was obtained via twice thermal shocking under similar current and voltage.

2.3. Electrochemical Measurements. All electrochemical tests were performed in a three-electrode cell connected to an electrochemical CHI 660E workstation. Ag/AgCl electrode, glass carbon electrode, and Pt plate served as the reference, working, and counter electrodes, respectively. The catalyst powder was added into the mixed solution of 800 μL of ethanol and 200 μL of Nafion (0.5 wt %), and then, the resulting mixture was subjected to ultrasonication for 30 min to obtain homogeneous catalyst ink. Next, 4 μL of catalyst ink was carefully loaded on the glassy carbon electrode and dried to prepare the working electrode. Based on the metal contents (ICP results) and the volume of ink, the Pt loading (m_{Pt}) of O−Pt_3Fe/rGO and D-Pt_3Fe/rGO−modified electrodes are highly comparable (16.92 vs 16.84 μg·cm^{-2}). The electrochemical active surface area (ECSA) was computed using the equation of ESCA = Q/(C·m), where Q represents the Coulombic charge of the H desorption peak, C is the hydrogen adsorption constant of Pt (210 μL cm^{-2}), and m refers to the mass of Pt covered on the electrode. Tests of ECSA were conducted in 0.5 M H_2SO_4 at 50 mV s^{-1}. To test the catalytic performance of EOR, cyclic voltammetry (CV) was performed from 50 mV s^{-1} in 1 M KOH containing 1 M ethanol. Linear sweep voltammetry (LSV) measurements were proceeded at 5 mV s^{-1} in 1 M KOH containing 1 M ethanol. Chronoamperometric (CA) investigation was performed in 1 M KOH containing 1 M ethanol at the potential of about 0.823 V for 3600 s for evaluating the stability of the catalysts. To further study the long-term stability, repeated CV scanning for 500 cycles from 0.1 to 1.5 V was conducted at 50 mV s^{-1} in 1 M KOH containing 1 M ethanol.

3. RESULTS AND DISCUSSION

3.1. Structural Characterizations. Scheme 1 displays the fabrication process of D-Pt_3Fe/rGO and O−Pt_3Fe/rGO. First, H_2PtCl_6·$6H_2O$, $Fe(CH_3COO)_2$, and GO were mixed and freeze dried to get a uniform Pt_3Fe/GO hydrogel. Subsequently, the hydrogel was subjected to the Joule heating treatment to ∼904 K within 2 s (temperature ramping rate is ∼0.3 × 10^3 K s^{-1}), allowing the formation of rGO-supported structurally disordered Pt_3Fe nanoalloys. From the heating curve (Figure S1), it can be seen that one-time thermal shock includes several heating and cooling cycles. Each cycle includes 2 s of heating (current-on), followed by several seconds of cooling period (current-off), attaining a peak temperature of approximately 904 K. Therefore, one-time thermal shock lasts several tens of seconds. Based on the results from EOR catalysis, two thermal shocks were selected as optimal condition for catalyst synthesis. Prolonged heating duration (>2 s) or an increased frequency of thermal shocks (exceeding twice) would result in a bigger size of alloy and a deterioration in EOR catalytic performance. The first thermal shock of just dozens of seconds may provide only limited energy and time for atomic diffusion of Pt and Fe, leading to the formation of disordered Pt_3Fe nanocrystals. When the second thermal shock was applied, the diffusion and rearrangement of building block atoms were promoted due to the extra energy and time input, promoting the occurrence of disorder-to-order phase transitions and formation of the O−Pt_3Fe/rGO.

Scheme 1. Schematic Diagram for the Preparation Process of Catalysts

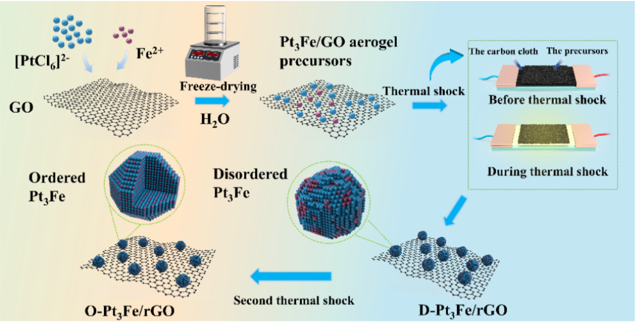

XRD profiles of D-Pt_3Fe/rGO and O−Pt_3Fe/rGO are shown in Figure 1a. Both profiles contain a broad peak for the (002) facet of carbonaceous supports near 25.6°.[33] D-Pt_3Fe/rGO reflections show five diffraction peaks between 40° and 90°, assignable to the (111), (200), (220), (311), and (222) planes of Pt_3Fe fcc phase.[34] Comparing with the patterns of pure Pt, these five peaks shifted to relatively higher angles (Figure S2) due to the concomitant lattice contraction upon the incorporation of Fe atoms with the smaller radius in Pt lattice.[35,36] Meanwhile, the peaks of (111), (200), (220), (311), and (222) in the O−Pt_3Fe/rGO profile exhibit positive shifts compared with those representing disordered Pt_3Fe alloys, disclosing a larger lattice strain in the O−Pt_3Fe/rGO compared with the D-Pt_3Fe/rGO. No patterns associated with pure Fe, Pt, or oxides are found, confirming the formation of the Pt_3Fe alloys and the structural purity of alloys. Moreover, the XRD profile of O−Pt_3Fe/rGO contains four new peaks at 22.9°, 32.7°, 52.8°, and 58.2°, which can be assigned to the characteristic (100), (110), (210), and (221) planes of ordered Pt_3Fe phase.[37,38] In addition, to evaluate the alloying degree of D-Pt_3Fe/rGO and O−Pt_3Fe/rGO, the induced lattice contraction and strain variation are evaluated based on the Debye−Scherrer equation.[39,40] The estimated strain variation in O−Pt_3Fe/rGO is higher than that D-Pt_3Fe/rGO (1.59% vs 0.53%), suggesting that the formation of ordered intermetallic phase results in a larger strain variation. The ordering degree of O−Pt_3Fe/rGO was assessed by comparing the peak intensities of (110) and (111) in the XRD profile, in accordance with the established technique.[41] In our study, the intensity ratio of the (110) peak to the (111) peak is 0.11, which approximates the standard value for Pt_3Fe intermetallic alloys (0.12, #JCPDS-892050). This suggests that the Pt_3Fe alloys in the O−Pt_3Fe/rGO have highly ordered intermetallic structures.

Raman spectra of GO, D-Pt_3Fe/rGO, and O−Pt_3Fe/rGO in Figure 1b exhibit typical D and G bands at ∼1348 and 1594 cm^{-1}, which denote the sp^3 hybridized defective graphite and the sp^2 hybridized ordered graphite.[42] The G bands of D-Pt_3Fe/rGO and O−Pt_3Fe/rGO shift to lower wavenumbers compared with that of GO, suggesting a strong interaction between rGO and metallic nanoparticles.[43,44−47] Besides, the I_D/I_G ratio of D-Pt_3Fe/rGO and O−Pt_3Fe/rGO are higher than that of raw GO (1.21, 0.94 and 0.83), suggesting that the in-plane sp^2 domains were decreased after the treatment by Joule heating.[48,49] This reveals that GO is effectively reduced and rGO is fundamentally built.[42] Such an effect is more noticeable for O−Pt_3Fe/rGO (the highest I_D/I_G ratio), indicating that the O−Pt_3Fe/rGO complex possesses more defects.

FTIR spectra were obtained to further reveal the change of chemical groups during the synthesis. Figure 1c displays the FT-IR spectra of GO, D-Pt_3Fe/rGO, and O−Pt_3Fe/rGO. The broad absorption peaks of all samples at approximately 3415 cm^{-1} are ascribed to the O−H stretching vibration.[50] For GO, the peaks between 1620 and 1750 cm^{-1} represent the stretching vibrations of C═O groups.[51] Other prominent peaks at 1053 cm^{-1} and 1225 cm^{-2} are attributed to the stretching vibrations of oxygen-containing functional groups such as C−O epoxy and C−O alkoxy groups.[43] Compared with the patterns of GO, the intensities of the peaks of O−H, C═O, C−O epoxy, and C−O alkoxy groups in the spectra of D-Pt_3Fe/rGO and O−Pt_3Fe/rGO are significantly reduced, suggesting the efficient reduction of GO to rGO.[42]

The porous structures of samples were examined by a nitrogen adsorption/desorption survey. Figure 1d demonstrates that both D-Pt_3Fe/rGO and O−Pt_3Fe/rGO show typical type-IV isotherms with apparent H_3 hysteresis loops,

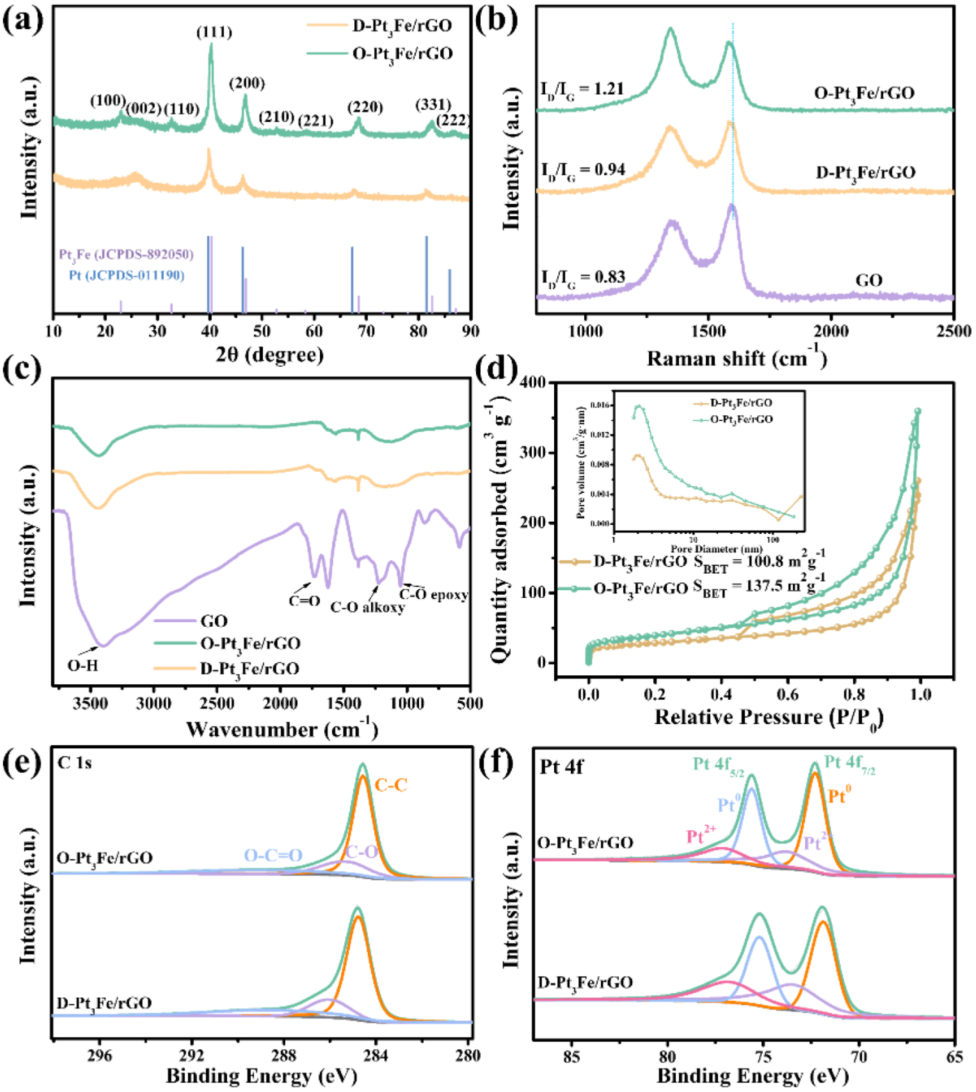

Figure 1. Structural characterizations of O−Pt_3Fe/rGO, D-Pt_3Fe/rGO and/or raw GO. (a) XRD profiles; (b) Raman spectra; (c) FTIR spectra; (d) N_2 adsorption−desorption isotherm and the pore size distribution (the inset); and (e−f) high-resolution C 1s and Pt 4f XPS spectra.

suggesting the existence of abundant mesopores and macropores.[52] O−Pt_3Fe/rGO possesses a larger surface area of 137.5 $m^2\ g^{-1}$ than D-Pt_3Fe/rGO (100.8 $m^2\ g^{-1}$). The pore size distributions were also estimated using the BJH method. As presented in the inset of Figure 1d, the average pore size of D-Pt_3Fe/rGO and O−Pt_3Fe/rGO is ∼21.9 nm and ∼19.3 nm, respectively, indicating that the mesopores are dominant in these two catalysts. The large surface area and the open pores of O−Pt_3Fe/rGO provide approachable active sites, which are beneficial for catalytic performance.[52]

XPS measurement was conducted to analyze the chemical valence states. As shown in Figure S3, the spectra of D-Pt_3Fe/rGO and O−Pt_3Fe/rGO contain four peaks at approximately 71, 284, 532, and 726 eV, which can be assigned to the Pt 4f, C 1s, O 1s and Fe 2p, respectively.[53] The high-resolution C 1s spectra of D-Pt_3Fe/rGO and O−Pt_3Fe/rGO (Figure 1e) were deconvoluted into three peaks, corresponding to C−C, C−O, and O—C═O bonds.[42,54] The fine Pt 4f spectrum of D-Pt_3Fe/rGO was resolved into two well-separated doublets, including two strong peaks at 71.86 and 75.18 eV for Pt^0 and another two relatively weak peaks at 73.49 and 76.81 eV for Pt^{2+} (Figure 1f).[55] Besides, the binding energies are positively shifted than those for metallic Pt, indicating the down-shifted Pt d-band center and the changed electronic structure upon Fe doping, which would weaken the CO adsorption.[55] As for the deconvoluted Pt 4f spectrum of O−Pt_3Fe/rGO, two peaks appeared at 72.28 and 75.60 eV correspond to Pt^0 and another two peaks emerged at 73.81 and 77.13 eV are related to Pt^{2+} (Figure 1f).[55] The presence of Pt^{2+} may attribute to the oxidation of the catalyst during synthesis or drying due to the incomplete removal of adsorbed H_2O. It might possibly result from catalysts that were partially oxidized when exposed to air during XPS studies. Similar XPS profiles containing Pt^{2+} signals have also been seen in certain Pt-based catalysts, indicating that Pt oxidation often occurs.[56,57] Moreover, it is noteworthy that the positive shift of ordered Pt_3Fe nanoparticles is larger than that of disordered Pt_3Fe nanoparticles, suggesting that there are more metallic interactions and electron transfer between Pt and Fe in ordered Pt_3Fe nanoparticles. Furthermore, the percentage of Pt^0 in D-Pt_3Fe/rGO and O−Pt_3Fe/rGO is much higher than that of Pt^{2+}. This confirms that a majority of the Pt precursors was reduced to metallic PtFe alloy nanoparticles, disclosing the effective reduction by thermal shock treatment. Additionally, the Pt^0/Pt^{2+} ratio of

O−Pt_3Fe/rGO is higher than that of D-Pt_3Fe/rGO. It has been reported that the high Pt^0/Pt^{2+} in catalysts is favorable for boosting the catalytic performance toward EOR as larger metallic state on the surface of catalysts would afford more free and effective Pt sites for oxidizing reactants.[41] Therefore, O−Pt_3Fe/rGO is expected to show better performance than D-Pt_3Fe/rGO.

The SEM image of O−Pt_3Fe/rGO in Figure 2a shows that the Pt_3Fe nanoparticles are well dispersed on the rGO carriers. TEM images in Figure 2b,c further confirm the ultrafine size and uniform dispersion. Figure 2d reveals that the average size of ordered Pt_3Fe is 3.7 nm. As disclosed in Figure 2e, O−Pt_3Fe/rGO displays an interplanar spacings of 0.378 nm, which is ascribed to the superlattice reflection of (100) of ordered Pt_3Fe.[37] The interplanar spacing of 0.218 nm is also found (Figure 2f), indexed to the (111) facet of Pt_3Fe alloys.[37] All these results confirm the formation of the ordered Pt_3Fe intermetallic phase in the O−Pt_3Fe/rGO sample, which agrees well with the XRD results. Meanwhile, the TEM-EDS elemental mapping images (Figure 2g1−g4) further display the coexistence of Pt, Fe, and C elements, which have uniform dispersion throughout the whole carbon networks. These results further reflect the formation of Pt_3Fe alloys. The ICP-MS analysis indicates that the Pt content in the oxidation reaction in O−Pt_3Fe/rGO is 14.95% and the atomic ratio of Pt/Fe is 2.91:1, respectively, which are close to the molar ratio of metals in the precursor and the stoichiometric composition of Pt_3Fe (Pt/Fe = 3:1), respectively.

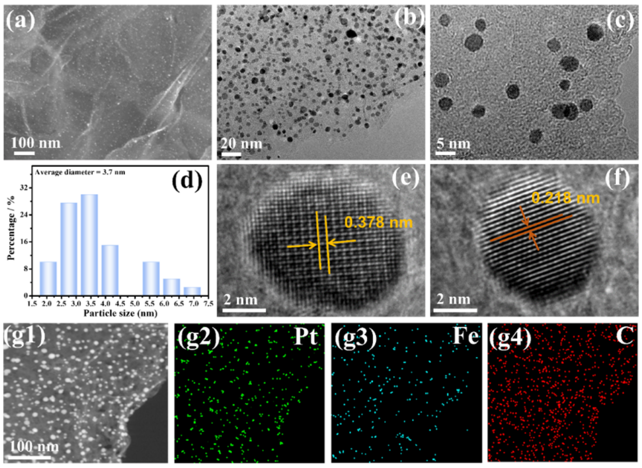

Figure 2. Morphology and microstructures of O−Pt_3Fe/rGO. (a) SEM image; (b, c) TEM images; (c, e, f) HRTEM images; (d) particle size distribution; and (g1−g4) corresponding elemental mapping images.

Figure S4 shows that D-Pt_3Fe/rGO exhibits a similar morphology to O−Pt_3Fe/rGO, with well-dispersed Pt_3Fe nanoparticles on rGO supports (Figure S4a,b). As shown in the inset of Figure S4b, the featured (111) lattice spacing of Pt_3Fe in D-Pt_3Fe/rGO is ∼0.221 nm, which is slightly larger than that of ordered Pt_3Fe (0.218 nm). This result confirms that the lattice strain is lower in D-Pt_3Fe/rGO, agreeing well with the XRD results. The TEM-EDS elemental mapping images (Figure S4e1-e4) prove the integration of Pt, Fe, and C elements in D-Pt_3Fe/rGO. Additionally, ICP-MS reveals that in D-Pt3Fe/rGO, the Pt loading is 14.88% and the Pt/Fe atomic ratio is 2.89:1. This result is similar to that of O−Pt_3Fe/rGO, indicating that both D-Pt_3Fe/rGO and O−Pt_3Fe/rGO synthesized by this strategy have a high raw material utilization rate.

3.2. Electrocatalytic Properties. The electrocatalytic properties of O−Pt_3Fe/rGO were evaluated in alkaline media, with D-Pt_3Fe/rGO and commercial Pt/C as comparative catalysts. The electrochemical tests details are provided in Section 2.3. Prior to the evaluation of catalytic performance, the electrochemical active surface areas (ECSAs) of samples were estimated in 0.5 M H_2SO_4 through cyclic voltammetry (CV). From the steady CV curves depicted in Figure S5, all catalysts display obvious hydrogen absorption and desorption peaks from 0.1 to 0.3 V, corresponding to the typical characteristics of Pt-based catalysts. The anodic peak at 0.8−1.1 V is attributed to the formation of Pt oxides, while the cathodic peak at ∼0.7 V refers to the corresponding reduction. Based on the CV curves, the ECSA of O−Pt_3Fe/rGO is 101.2 $m^2\ g^{-1}$, which is much higher than those of D-Pt_3Fe/rGO (84.9 $m^2\ g^{-1}$) and Pt/C (60.8 $m^2\ g^{-1}$) (Figure 3a). These data suggest that O−Pt_3Fe/rGO possesses more active sites than D-Pt_3Fe/rGO and Pt/C, thus leading to enhanced catalytic activity.

To evaluate the EOR performance, CV surveys were implemented in 1 M KOH containing 0.5 M ethanol. Figure 3b shows that the CV curves of three catalysts contain two oxidation peaks: The broader peak in the forward scan (I_F) corresponds to the oxidation of ethanol into intermediates and the narrower peak in the backward scan with (I_B) corresponds to further oxidation of intermediates. Based on the above-mentioned results, the mass activity of the O−Pt_3Fe/rGO was estimated to be 5.66 A mg_{Pt}^{-1}, which was 2.5 and 7.1 times higher than those of the D-Pt_3Fe/rGO (2.29 A mg_{Pt}^{-1}) and Pt/C (0.8 A mg_{Pt}^{-1}), respectively. The specific activity (Figure 3c) was also obtained based on the ECSA-normalized CV curves (Figure S6). The data indicated that O−Pt_3Fe/rGO exhibited the best performance among all three catalysts, with a specific activity of 5.6 mA cm^{-2} (2.1 and 4.3 times higher than those of D-Pt_3Fe/rGO and Pt/C, respectively). Meanwhile, the present EOR performance of O−Pt_3Fe/rGO was compared with some recently reported Pt-based catalysts. As demonstrated in Figure 3d and reported in Table S1, the O−Pt_3Fe/rGO exhibits impressive mass and specific activity, exceeding that of many previously reported Pt-based bimetallic (PtPd NDs, Pt_3Cu/graphene, AgPt (1:3)/C, PtMo/C, $Pt_{68}Cu_{32}$ nanoalloys, 250_$Pt_{0.5}Rh_{0.5}$, PtPd/G-40, and PtCu NC/CB) and trimetallic catalysts (PtPbPd NWs, PtRh@SnO_2 NW/C, PtRu@SnO_2 NW/C, PdPtNi PNSs, and PtPdRh/CNTs) for EOR. This remarkable performance implies that the O−Pt_3Fe/rGO catalyst achieves a high Pt utilization rate, which makes it promising in DEFC utilization. We conducted the relative test in acidic conditions. As seen in Figure S7, despite the inferior performance of all three catalysts in acidic conditions relative to alkaline conditions, O−Pt_3Fe/rGO with ordered nanoalloys still exhibits the best activity among all three catalysts, showing the highest mass activity and specific activity of 1.39 A mg_{Pt}^{-1} and 1.38 mA cm^{-2}.

To analyze the kinetic process, the LSV behavior of three catalysts was studied in 1 M KOH containing 0.5 M ethanol in a potential range of 0.1−0.5 V. As shown in Figure 3e, O−Pt_3Fe/rGO exhibits a more negative onset potential of ∼431 mV, which is 22 mV and 153 mV lower than those of D-Pt_3Fe/rGO and Pt/C, respectively, indicating that the effectiveness of Fe dopants and ordered intermetallic structures. Tafel plots were given to further analyze the electrocatalytic kinetics of the

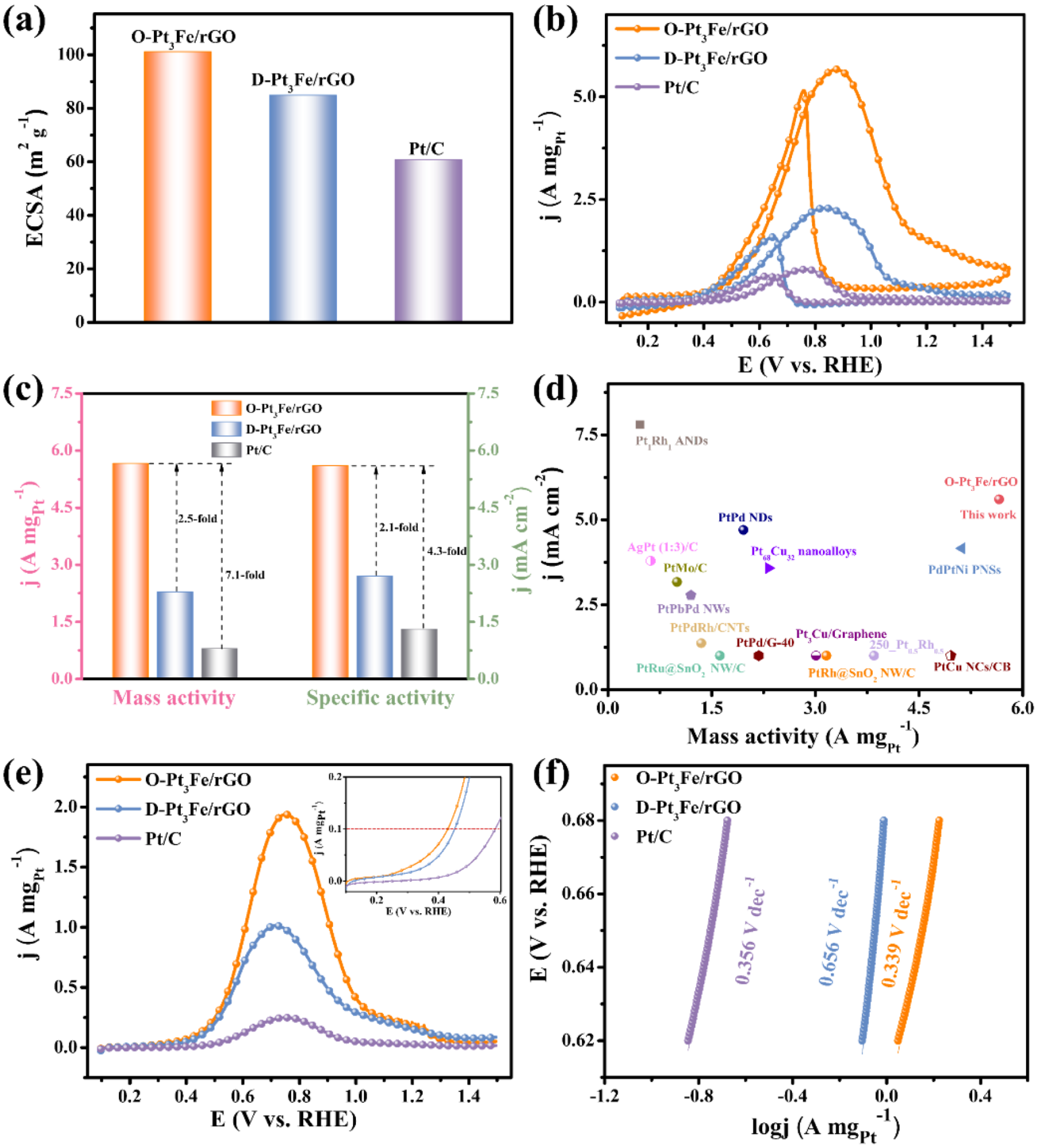

Figure 3. EOR performance of all catalysts. (a) ECSA values; (b) mass-normalized CV curves; (c) mass activity and specific activity; (d) EOR performance comparison of O−Pt_3Fe/rGO and other Pt-based catalysts; (e) LSV curves (scan rate: 5 mVs^{-1}), the inset provides enlarged curves presented in (e); and (f) Tafel plots.

three catalysts. As shown in Figure 3f, the Tafel slopes for O−Pt_3Fe/rGO, D-Pt_3Fe/rGO. and Pt/C are 0.656 V dec^{-1}, 0.339 V dec^{-1}, and 0.356 V dec^{-1}, respectively. The smallest Tafel slope of the diffraction-induced reaction of the syringe of the O−Pt_3Fe/rGO means that the reaction kinetics is significantly enhanced during the EOR process.

For the investigation of durability, chronoamperometry (CA) was conducted to record the consecutive current density of ethanol oxidation at 0.80 V. As shown in Figure 4a, there is a drastic reduction of current density during the incipient stage, which can be put down to the carbonaceous intermediates generated at the initial stage of the ethanol oxidation.[58,59] As the reaction proceeds, the adsorption and oxidation rates of the carbonaceous intermediates on active sites achieve a state of equilibrium, and thus, the current density is inclined to be steady.[58] Clearly, the O−Pt_3Fe/rGO displays the slowest rate of current degradation in the incipient stage and the largest current density during the whole period among all the catalysts. Besides, as displayed in Figure 4b, after 3600 s, the reversible mass activity of O−Pt_3Fe/rGO shows the largest normalized current density of and residual mass activity of 3.7% and 0.23 A mg_{Pt}^{-1}, much larger than those of D-Pt_3Fe/rGO (1.6%, 0.05 A mg_{Pt}^{-1}) and Pt/C (1.4%, 0.01 A mg_{Pt}^{-1}).

Additionally, the stability was also evaluated by 500 continuous CV scans between 0.1 and 1.5 V. Figure 4c demonstrates that the mass activity of all catalysts decreases as the number of CV cycles increase. Nevertheless, compared with D-Pt_3Fe/rGO and Pt/C, the decay of the cation of the

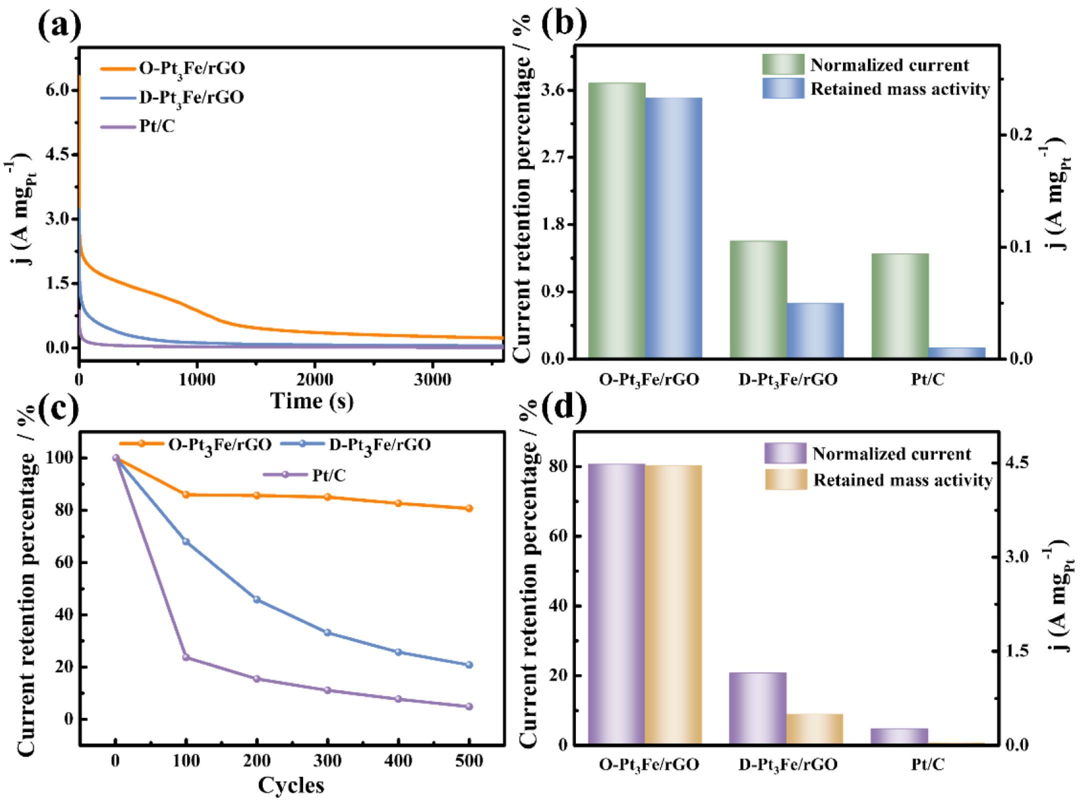

Figure 4. Stability of all catalysts toward EOR. (a) CA curves; (b) normalized current and retained mass activity after 3600 s; (c) normalized current vs cycle number; and (d) normalized current and mass activity after 500 cycles.

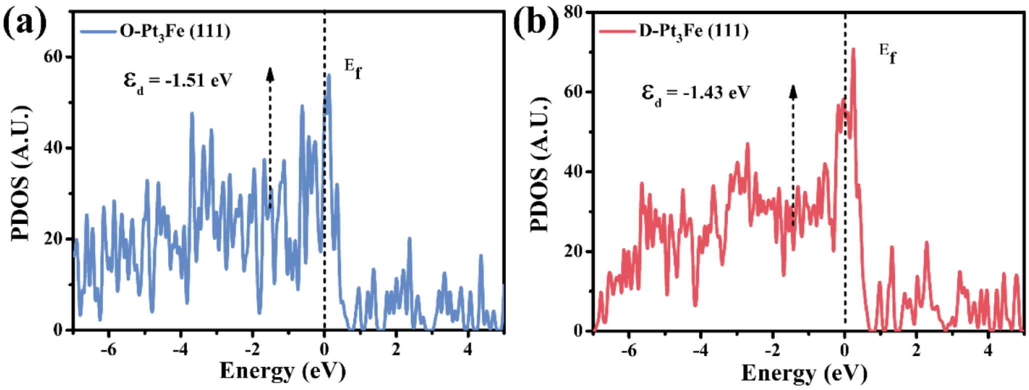

Figure 5. PDOS of the Pt d-band of (a) O−Pt$_3$Fe and (b) D-Pt$_3$Fe.

tetrahydride nitrate in the O−Pt$_3$Fe/rGO complex is always the lowest during the entire process. As shown in Figure 4d, after 500 cycles, the retention rate of current density of O−Pt$_3$Fe/rGO is up to 80.7%, while much lower retention rate is seen for D-Pt$_3$Fe/rGO (20.8%) and Pt/C (4.8%). Besides, O−Pt$_3$Fe/rGO also shows a much higher retained mass activity of 4.46 A mg$_{Pt}$$^{-1}$ than D-Pt$_3$Fe/rGO (0.05 A mg$_{Pt}$$^{-1}$) and Pt/C (0.01 A mg$_{Pt}$$^{-1}$), indicating its superior durability among all the catalysts.

3.3. Mechanism Analysis. To unravel the mechanism of the enhanced EOR activity of the O−Pt$_3$Fe/rGO, DFT calculations were performed. The projected density of states (PDOS) of the d-orbitals were first calculated to determine the d-band center and unveil the modification of the electronic structure. Figure 5 depicts that O−Pt$_3$Fe (111) has a lower d-band center of −1.51 eV than D-Pt$_3$Fe (111) (−1.43 eV), which would attenuate the CO adsorption on O−Pt$_3$Fe (111) and aid in the renewal of Pt active sites.[60] Therefore, the calculation results of the Pt d-band imply that the stronger strain and ordering effect can optimize the electronic property, leading to enhanced EOR kinetics.

Apart from the d-band analysis, the CO adsorption energies on model disordered and ordered catalysts with (111) crystalline facets were also estimated. Figure 6a,b reveals that the CO adsorption energy on D-Pt$_3$Fe (111) and O−Pt$_3$Fe (111) is −2.78 eV and-1.55 eV, respectively, suggesting a weaker adsorption of CO on O−Pt$_3$Fe (111). These data imply that the desorption of CO on O−Pt$_3$Fe (111) is more favorable.[61] Therefore, the catalysts with ordered Pt$_3$Fe nanoalloys are capable of showing better catalytic performance. The adsorption energy of OH on both surfaces was also analyzed since it is deemed as another key descriptor of EOR

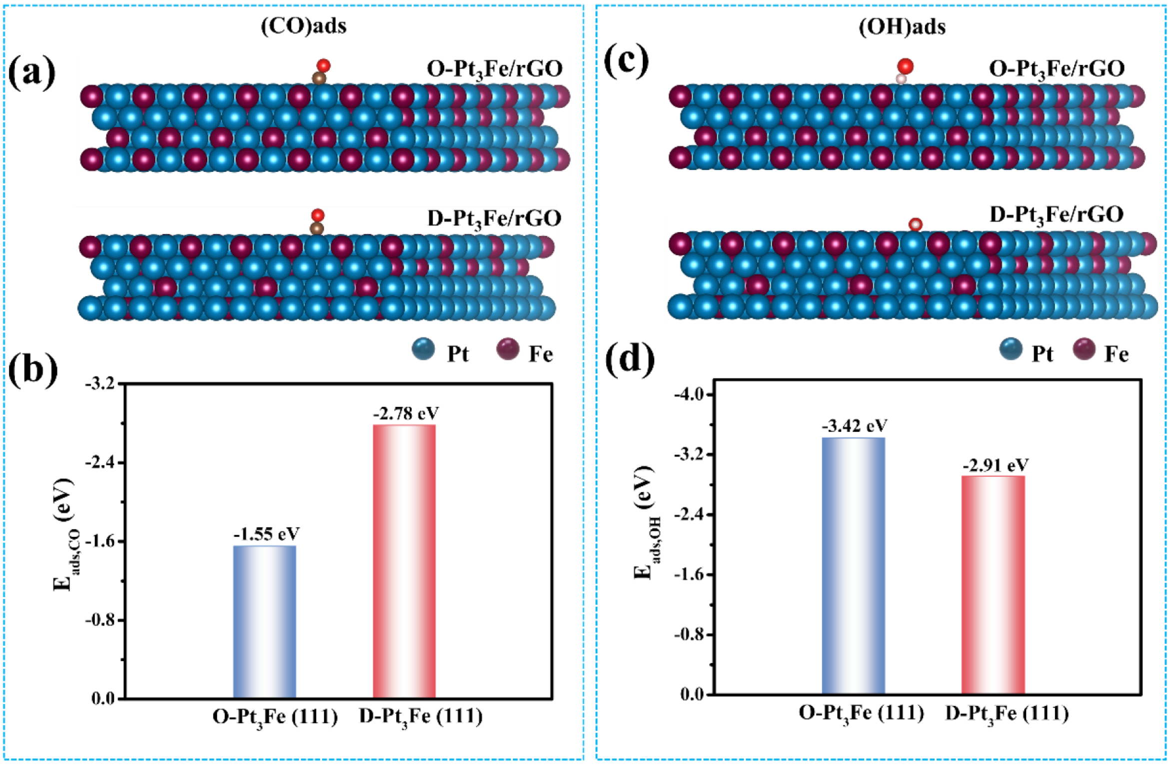

Figure 6. (a, b) The atomic structures (side view) for the adsorption of CO on O−Pt_3Fe (111) and D-Pt_3Fe (111) and the corresponding CO adsorption energies; (c, d) the atomic structures (side view) for the adsorption of OH on O−Pt_3Fe (111) and D-Pt_3Fe (111) and the corresponding OH adsorption energies.

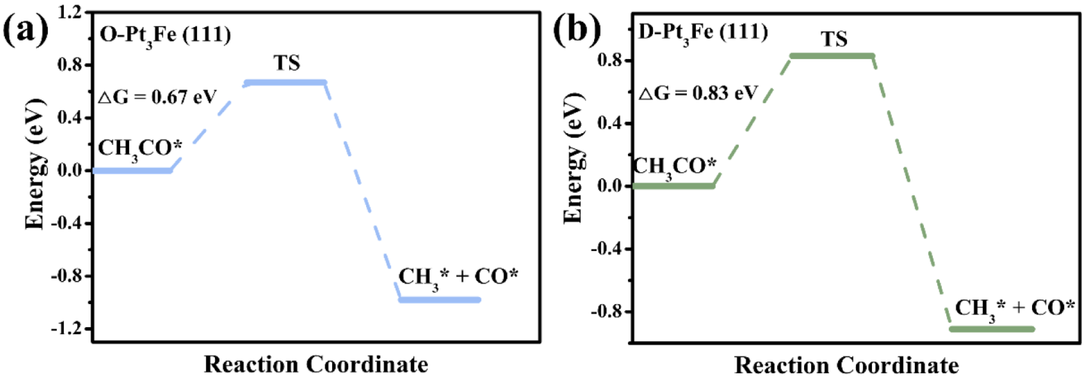

Figure 7. DFT-calculated reaction energy barriers for C−C scission on the 111-nm ion of (a) O−Pt_3Fe and (b) the 111 nm ion of (d) D-Pt_3Fe (111).

catalytic activity.[62] Figure 6c,d unveils that the OH adsorption energy on D-Pt_3Fe (111) and O−Pt_3Fe (111) surfaces is −2.91 eV and −3.42 eV, respectively, indicating the OH adsorption on O−Pt_3Fe (111) is more prone.[61] The higher OH affinity is attributed to the more constrained lattice structure of ordered Pt_3Fe.

Given that the decomposition of CH_3CO^* (the cleavage of C−C bond) has generally been considered as the rate-determining step in the ethanol oxidation,[63,64] the energy barriers for CH_3CO^* decomposition on D-Pt_3Fe (111) and O−Pt_3Fe (111) were also calculated (Figures S8 and 7). Figure 7a shows that the cleavage of the C−C bond on D-Pt_3Fe (111) exhibited an energy threshold of 0.83 eV, while a lower energy barrier of 0.67 eV was required on the C−C bond on O−Pt_3Fe (111) (Figure 7b). This suggested that the stronger strain and ordering effect of Pt_3Fe intermetallic compounds play important roles in promoting the scission of the C−C bond.

By integration of the abovementioned DFT calculations and experimental results, the EOR mechanism of O−Pt_3Fe/rGO can be deduced (Scheme 2). The incorporation of Fe in ordered lattice structure brings about the strain effect and short-range electron transfer (ligand effect), leading to the weakened adsorption of CO on Pt and the regeneration of Pt active sites. Besides, due to the bifunctional effect, alloying Pt with transition metal can afford more absorbed OH at lower potential than on pure Pt. The ordered Pt_3Fe enables enhanced OH adsorption, thereby accelerating the removal of CO and other intermediates and contributing to enhanced reaction kinetics. Moreover, the ordered Pt_3Fe has exceptional ability for C−C cleavage, which would also improve the catalytic activity.

Scheme 2. Catalytic Mechanism of O−Pt_3Fe/rGO toward EOR

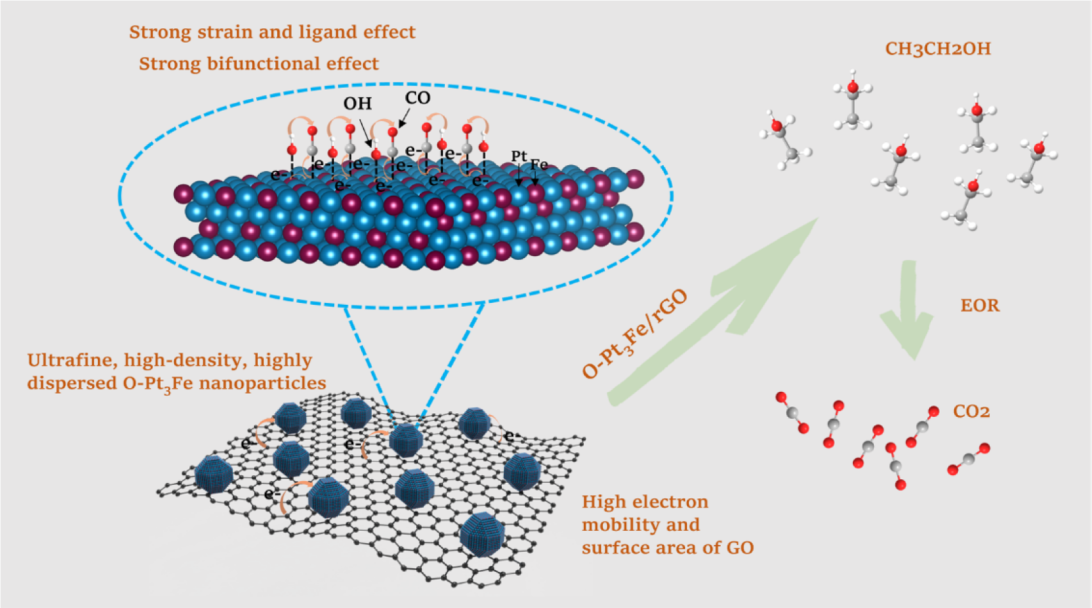

4. CONCLUSIONS

In summary, we displayed an ultrafast fabrication of ordered Pt_3Fe intermetallic nanocrystals anchored on rGO composites toward ethanol oxidation. The ordered Pt_3Fe exhibits a sub−5-nm particle size on the rGO support, with high density and uniformity. The structural regulation between ordered and disordered intermetallic phases can be easily achieved by tuning the parameters in the thermal shock synthesis. Compared with the commercial Pt/C and the counterpart D-Pt_3Fe/rGO, O−Pt_3Fe/rGO delivers excellent mass activity and specific activity of 5.66 A mg^{-1} and 5.60 mA cm^{-2}, which are also superior to many recently reported Pt alloy−based catalysts for EOR. O−Pt_3Fe/rGO also exhibits the lowest-onset potential, the smallest Tafel slope, and the best aging resistance among all three catalysts, reflecting the greatly enhanced reaction kinetics on it. DFT calculations reveal that the O−Pt_3Fe/rGO exhibits a lower d-band center, a weakened adsorption of CO, an enhanced adsorption of OH, and a lower energy barrier for C−C bond cleavage, therefore resulting in a superior overall performance. Our report gives a promising strategy for the facile construction of ultrafine intermetallic electrocatalysts for direct ethanol fuel cell and other related conversion of renewable energy.

■ ASSOCIATED CONTENT

Supporting Information

The Supporting Information is available free of charge at https://pubs.acs.org/doi/10.1021/acssuschemeng.4c06241.

Part of the experimental section, DFT calculations, XRD, XPS, SEM, TEM, and EOR catalytic performance (PDF)

■ AUTHOR INFORMATION

Corresponding Authors

Wei Gan − *Shenzhen Key Laboratory of Flexible Printed Electronics Technology, and School of Science, Harbin Institute of Technology (Shenzhen), Shenzhen 518055, China; School of Chemistry and Chemical Engineering, Harbin Institute of Technology, Harbin 150001, China;* orcid.org/0000-0001-8481-122X; Email: ganwei@hit.edu.cn

Qunhui Yuan − *Shenzhen Key Laboratory of Flexible Printed Electronics Technology, and School of Materials Science and Engineering, Harbin Institute of Technology (Shenzhen), Shenzhen 518055, China*; Email: yuanqunhui@hit.edu.cn

Authors

Mingxing Nie − *Shenzhen Key Laboratory of Flexible Printed Electronics Technology, and School of Science, Harbin Institute of Technology (Shenzhen), Shenzhen 518055, China; School of Chemistry and Chemical Engineering, Harbin Institute of Technology, Harbin 150001, China*

Zijian Wang − *Shenzhen Key Laboratory of Flexible Printed Electronics Technology, and School of Materials Science and Engineering, Harbin Institute of Technology (Shenzhen), Shenzhen 518055, China*

Dongxuan He − *Shenzhen Key Laboratory of Flexible Printed Electronics Technology, and School of Materials Science and Engineering, Harbin Institute of Technology (Shenzhen), Shenzhen 518055, China*

Complete contact information is available at: https://pubs.acs.org/10.1021/acssuschemeng.4c06241

Notes

The authors declare no competing financial interest.

■ ACKNOWLEDGMENTS

This work was financially supported by the fundamental research fund from Shenzhen (JCYJ20220531095214032).

■ REFERENCES

(1) Khan, K.; Su, C. W.; Khurshid, A.; Qin, M. Does energy security improve renewable energy? A geopolitical perspective. *Energy* **2023**, *282*, 128824.

(2) Liu, J.; Huang, Z. Y.; Fan, M.; Yang, J. H.; Xiao, J.; Wang, Y. Future energy infrastructure, energy platform and energy storage. *Nano Energy* **2022**, *104*, 107915.

(3) Yan, C.; Liu, Y.-L.; Zeng, Q.; Wang, G.-G.; Han, J.-C. 2D Nanomaterial Supported Single-Metal Atoms for Heterogeneous Photo/Electrocatalysis. *Adv. Funct. Mater.* **2023**, *33* (5), 2210837.

(4) Fan, L. X.; Tu, Z. K.; Chan, S. H. Recent development of hydrogen and fuel cell technologies: A review. *Energy Rep.* **2021**, *7*, 8421−8446.

(5) Li, C.; Wang, K.; Xie, D. A review of approaches for the design of high-performance electrocatalysts for ethanol electrooxidation. *Surf. Interfaces* **2022**, *28*, 101594.

(6) Lv, F.; Zhang, W.; Sun, M.; Lin, F.; Wu, T.; Zhou, P.; Yang, W.; Gao, P.; Huang, B.; Guo, S. Au Clusters on Pd Nanosheets Selectively Switch the Pathway of Ethanol Electrooxidation: Amorphous/Crystalline Interface Matters. *Adv. Energy Mater.* **2021**, *11* (19), 2100187.

(7) Pham, H. Q.; Huynh, T. T.; Pham, T. M.; Ho, V. T. T. Boosting alcohol electro-oxidation reaction with bimetallic PtRu nanoalloys supported on robust $Ti_{0.7}W_{0.3}O_2$ nanomaterial in direct liquid fuel cells. *Int. J. Hydrogen Energy* **2021**, *46* (31), 16776−16786.

(8) Li, M. G.; Zhao, Z. L.; Xia, Z. H.; Yang, Y.; Luo, M. C.; Huang, Y. R.; Sun, Y. J.; Chao, Y. G.; Yang, W. X.; Yang, W. W.; Yu, Y. S.; Lu, G.; Guo, S. J. Lavender-Like Ga-Doped Pt_3Co Nanowires for Highly Stable and Active Electrocatalysis. *ACS Catal.* **2020**, *10* (5), 3018−3026.

(9) Rizo, R.; Bergmann, A.; Timoshenko, J.; Scholten, F.; Rettenmaier, C.; Jeon, H. S.; Chen, Y.-T.; Yoon, A.; Bagger, A.; Rossmeisl, J.; et al. Pt-Sn-Co nanocubes as highly active catalysts for ethanol electro-oxidation. *J. Catal.* **2021**, *393*, 247−258.

(10) Li, S. W.; Shu, J. H.; Ma, S. Z.; Yang, H. L.; Jin, J.; Zhang, X. H.; Jin, R. F. Engineering three-dimensional nitrogen-doped carbon black embedding nitrogen-doped graphene anchoring ultrafine surface-clean Pd nanoparticles as efficient ethanol oxidation electrocatalyst. *Appl. Catal., B* **2021**, *280*, 119464.

(11) Rodríguez-Gómez, A.; Lepre, E.; Sánchez-Silva, L.; López-Salas, N.; de la Osa, A. R. PtRu nanoparticles supported on noble carbons for ethanol electrooxidation. *J. Energy Chem.* **2022**, *66*, 168−180.

(12) Gómez-Monsiváis, A. C.; Velázquez-Hernández, I.; Alvarez-Contreras, L.; Guerra-Balcázar, M.; Arriaga, L. G.; Arjona, N.; Ledesma-García, J. In Situ Surface-Enhanced Raman Spectroscopy Study of the Electrocatalytic Effect of PtFe/C Nanocatalyst on Ethanol Electro-Oxidation in Alkaline Medium. *Energies* **2017**, *10* (3), 290.

(13) Zhang, Y. P.; Gao, F.; Song, T. X.; Wang, C.; Chen, C. Y.; Du, Y. K. Novel networked wicker-like PtFe nanowires with branch-rich exteriors for efficient electrocatalysis. *Nanoscale* **2019**, *11* (33), 15561−15566.

(14) Wang, P.; Yin, S. B.; Wen, Y.; Tian, Z. Q.; Wang, N. Z.; Key, J. L.; Wang, S. B.; Shen, P. K. Ternary Pt_9RhFe_x Nanoscale Alloys as Highly Efficient Catalysts with Enhanced Activity and Excellent CO-Poisoning Tolerance for Ethanol Oxidation. *ACS Appl. Mater. Interfaces* **2017**, *9* (11), 9584−9591.

(15) He, Z. L.; Huang, X. X.; Chen, Q. W.; Zhai, C. Y.; Hu, Y. F.; Zhu, M. S. Pt nanoclusters embedded Fe-based metal-organic framework as a dual-functional electrocatalyst for hydrogen evolution and alcohols oxidation. *J. Colloid Interface Sci.* **2022**, *616*, 279−286.

(16) Song, P. P.; Xu, H.; Wang, J.; Zhang, Y. P.; Gao, F.; Guo, J.; Shiraishi, Y.; Du, Y. K. 1D alloy ultrafine Pt-Fe nanowires as efficient electrocatalysts for alcohol electrooxidation in alkaline media. *Nanoscale* **2018**, *10* (35), 16468−16473.

(17) Wang, C.; Xu, H.; Gao, F.; Zhang, Y. P.; Song, T. X.; Wang, C. Q.; Shang, H. Y.; Zhu, X.; Du, Y. K. High-density surface protuberances endow ternary PtFeSn nanowires with high catalytic performance for efficient alcohol electro-oxidation. *Nanoscale* **2019**, *11* (39), 18176−18182.

(18) Hu, Y. Z.; Shen, T.; Zhao, X. R.; Zhang, J. J.; Lu, Y.; Shen, J.; Lu, S. F.; Tu, Z. K.; Xin, H. L. L.; Wang, D. L. Combining structurally ordered intermetallics with N-doped carbon confinement for efficient and anti-poisoning electrocatalysis. *Appl. Catal., B* **2020**, *279*, 119370.

(19) Xiao, W. P.; Lei, W.; Gong, M. X.; Xin, H. L.; Wang, D. L. Recent Advances of Structurally Ordered Intermetallic Nanoparticles for Electrocatalysis. *ACS Catal.* **2018**, *8* (4), 3237−3256.

(20) Chen, H. S.; Benedetti, T. M.; Lian, J. X.; Cheong, S.; O'Mara, P. B.; Sulaiman, K. O.; Kelly, C. H. W.; Scott, R. W. J.; Gooding, J. J.; Tilley, R. D. Role of the Secondary Metal in Ordered and Disordered Pt-M Intermetallic Nanoparticles: An Example of Pt_3Sn Nanocubes for the Electrocatalytic Methanol Oxidation. *ACS Catal.* **2021**, *11* (4), 2235−2243.

(21) Liang, L.; Li, M.; Zhang, B.; Liang, J.; Zeng, B.; Wang, L.; Tang, Y.; Fu, G.; Cui, Z. Ordered and Isolated Pd Sites Endow Antiperovskite-Type $PdFe_3N$ with High CO-Tolerance for Formic Acid Electrooxidation. *Adv. Energy Mater.* **2023**, *13* (10), 2203803.

(22) Rössner, L.; Armbrüster, M. Electrochemical Energy Conversion on Intermetallic Compounds: A Review. *ACS Catal.* **2019**, *9* (3), 2018−2062.

(23) Yan, Y.; Du, J. S.; Gilroy, K. D.; Yang, D.; Xia, Y.; Zhang, H. Intermetallic Nanocrystals: Syntheses and Catalytic Applications. *Adv. Mater.* **2017**, *29* (14), 1605997.

(24) Zhang, B. T.; Fu, G. T.; Li, Y. T.; Liang, L. C.; Grundish, N. S.; Tang, Y. W.; Goodenough, J. B.; Cui, Z. M. General Strategy for Synthesis of Ordered Pt_3M Intermetallics with Ultrasmall Particle Size. *Angew. Chem., Int. Ed.* **2020**, *59* (20), 7857−7863.

(25) Kim, H. Y.; Joo, S. H. Recent advances in nanostructured intermetallic electrocatalysts for renewable energy conversion reactions. *J. Mater. Chem. A* **2020**, *8* (17), 8195−8217.

(26) Chen, H.; Wang, D. L.; Yu, Y. C.; Newton, K. A.; Muller, D. A.; Abruña, H.; DiSalvo, F. J. A Surfactant-Free Strategy for Synthesizing, and Processing Intermetallic Platinum-Based Nanoparticle Catalysts. *J. Am. Chem. Soc.* **2012**, *134* (44), 18453−18459.

(27) Luo, M.; Sun, Y.; Wang, L.; Guo, S. Tuning Multimetallic Ordered Intermetallic Nanocrystals for Efficient Energy Electrocatalysis. *Adv. Energy Mater.* **2017**, *7* (11), 1602073.

(28) Cui, M.; Yang, C.; Hwang, S.; Yang, M.; Overa, S.; Dong, Q.; Yao, Y.; Brozena, A. H.; Cullen, D. A.; Chi, M.; et al. Multi-principal elemental intermetallic nanoparticles synthesized via a disorder-to-order transition. *Sci. Adv.* **2022**, *8* (4), No. eabm4322.

(29) Cui, M. J.; Yang, C. P.; Hwang, S.; Li, B. Y.; Dong, Q.; Wu, M. L.; Xie, H.; Wang, X. Z.; Wang, G. F.; Hu, L. B. Rapid Atomic Ordering Transformation toward Intermetallic Nanoparticles. *Nano Lett.* **2022**, *22* (1), 255−262.

(30) Yan, W.; Wang, X.; Liu, M.; Ma, K.; Wang, L.; Liu, Q.; Wang, C.; Jiang, X.; Li, H.; Tang, Y.; et al. PCTS-Controlled Synthesis of $L1_0/L1_2$-Typed Pt-Mn Intermetallics for Electrocatalytic Oxygen Reduction. *Adv. Funct. Mater.* **2024**, *34* (6), 2310487.

(31) Li, J. R.; Jilani, S. A.; Lin, H. H.; Liu, X. M.; Wei, K. C.; Jia, Y. K.; Zhang, P.; Chi, M. F.; Tong, Y. Y.; Xi, Z.; Sun, S. H. Ternary CoPtAu Nanoparticles as a General Catalyst for Highly Efficient Electro-oxidation of Liquid Fuels. *Angew. Chem., Int. Ed.* **2019**, *58* (33), 11527−11533.

(32) Feng, F.; Ma, C.; Han, S.; Ma, X.; He, C.; Zhang, H.; Cao, W.; Meng, X.; Xia, J.; Zhu, L.; et al. Breaking Highly Ordered PtPbBi Intermetallic with Disordered Amorphous Phase for Boosting Electrocatalytic Hydrogen Evolution and Alcohol Oxidation. *Angew. Chem., Int. Ed.* **2024**, *63* (25), No. e202405173.

(33) Zhang, Q.; Jiang, L.; Wang, H.; Liu, J. L.; Zhang, J. F.; Zheng, Y. Q.; Li, F. T.; Yao, C. X.; Hou, S. F. Hollow Graphitized Carbon Nanocage Supported Pd Catalyst with Excellent Electrocatalytic Activity for Ethanol Oxidation. *ACS Sustainable Chem. Eng.* **2018**, *6* (6), 7507−7514.

(34) Kuang, P.; Ni, Z.; Zhu, B.; Lin, Y.; Yu, J. Modulating the d-Band Center Enables Ultrafine Pt_3Fe Alloy Nanoparticles for pH-Universal Hydrogen Evolution Reaction. *Adv. Mater.* **2023**, *35* (41), 2303030.

(35) An, H. M.; Zhao, Z. L.; Wang, Q.; Zhang, L. Y.; Gu, M.; Li, C. M. Ternary PtPdCu Multicubes as a Highly Active and Durable Catalyst toward the Oxygen Reduction Reaction. *ChemElectrochem* **2018**, *5* (10), 1345−1349.

(36) Liu, W.; Wang, P.; Wang, Z. H. PtPdCu cubic nanoframes as electrocatalysts for methanol oxidation reaction. *CrystEngcomm* **2021**, *23* (45), 7978−7984.

(37) Chen, L.; Bock, C.; Mercier, P. H. J.; MacDougall, B. R. Ordered alloy formation for Pt_3Fe/C, PtFe/C and $Pt_{5.75}Fe_{5.75}Cu_y/CO_2$-reduction electro-catalysts. *Electrochim. Acta.* **2012**, *77*, 212−224.

(38) Lin, C. X.; Huang, Z. Q.; Zhang, Z. Y.; Zeng, T.; Chen, R. Z.; Tan, Y. Y.; Wu, W.; Mu, S. C.; Cheng, N. C. Structurally Ordered Pt_3Co Nanoparticles Anchored on N-Doped Graphene for Highly Efficient Hydrogen Evolution Reaction. *ACS Sustainable Chem. Eng.* **2020**, *8* (45), 16938−16945.

(39) Wang, Q. M.; Chen, S. G.; Lan, H. Y.; Li, P.; Ping, X. Y.; Ibraheem, S.; Long, D. J.; Duan, Y. J.; Wei, Z. D. Thermally driven interfacial diffusion synthesis of nitrogen-doped carbon confined trimetallic Pt_3CoRu composites for the methanol oxidation reaction. *J. Mater. Chem. A* **2019**, *7* (30), 18143−18149.

(40) Wang, Q. M.; Chen, S. G.; Li, P.; Ibraheem, S.; Li, J.; Deng, J. H.; Wei, Z. D. Surface Ru enriched structurally ordered intermetallic PtFe@PtRuFe core-shell nanostructure boosts methanol oxidation reaction catalysis. *Appl. Catal., B* **2019**, *252*, 120−127.

(41) Nie, Y.; Qi, X. Q.; Wu, R.; Yang, R. L.; Wang, H.; Deng, M.; Zhang, S.; Lu, S.; Gu, Z. R.; Liu, X. T. Structurally ordered PtFe intermetallic nanocatalysts toward efficient electrocatalysis of methanol oxidation. *Appl. Surf. Sci.* **2021**, *569*, 151004.

(42) Li, S. S.; Zheng, J. N.; Ma, X. H.; Hu, Y. Y.; Wang, A. J.; Chen, J. R.; Feng, J. J. Facile synthesis of hierarchical dendritic PtPd nanogarlands supported on reduced graphene oxide with enhanced electrocatalytic properties. *Nanoscale* **2014**, *6* (11), 5708−5713.

(43) Esabattina, S.; Posa, V. R.; Zhanglian, H.; Godlaueeti, S. K.; Reddy, R. R. N.; Somala, A. R. Fabrication of bimetallic PtPd alloy nanospheres supported on rGO sheets for superior methanol electro-oxidation. *Int. J. Of Hydrogen Energy* **2018**, *43* (8), 4115−4124.

(44) Fang, W.; Hsu, A. L.; Caudillo, R.; Song, Y.; Birdwell, A. G.; Zakar, E.; Kalbac, M.; Dubey, M.; Palacios, T.; Dresselhaus, M. S.; Araujo, P. T.; Kong, J. Rapid Identification of Stacking Orientation in Isotopically Labeled Chemical-Vapor Grown Bilayer Graphene by Raman Spectroscopy. *Nano Lett.* **2013**, *13* (4), 1541−1548.

(45) Liu, M. M.; Lu, Y. Z.; Chen, W. PdAg Nanorings Supported on Graphene Nanosheets: Highly Methanol-Tolerant Cathode Electrocatalyst for Alkaline Fuel Cells. *Adv. Funct. Mater.* **2013**, *23* (10), 1289−1296.

(46) Zhang, H.; Xu, X. Q.; Gu, P.; Li, C. Y.; Wu, P.; Cai, C. X. Microwave-assisted synthesis of graphene-supported Pd_1Pt_3 nanostructures and their electrocatalytic activity for methanol oxidation. *Electrochim. Acta.* **2011**, *56* (20), 7064−7070.

(47) Zhang, H. F.; Ren, W. N.; Guan, C.; Cheng, C. W. Pt decorated 3D vertical graphene nanosheet arrays for efficient methanol oxidation and hydrogen evolution reactions. *J. Mater. Chem. A* **2017**, *5* (41), 22004−22011.

(48) Ferrari, A. C.; Meyer, J. C.; Scardaci, V.; Casiraghi, C.; Lazzeri, M.; Mauri, F.; Piscanec, S.; Jiang, D.; Novoselov, K. S.; Roth, S.; Geim, A. K. Raman spectrum of graphene and graphene layers. *Phys. Rev. Lett.* **2006**, *97* (18), 187401.

(49) Sheka, E. F.; Golubev, Y. A.; Popova, N. A. Graphene Domain Signature of Raman Spectra of sp^2 Amorphous Carbons. *Nanomaterials* **2020**, *10* (10), 2021.

(50) Ma, Y. S.; Du, K. F.; Guo, Y. F.; Tang, M. Y.; Yin, H. Y.; Mao, X. H.; Wang, D. H. Biphase Co@C core-shell catalysts for efficient Fenton-like catalysis. *J. Hazard. Mater.* **2022**, *429*, 128287.

(51) Pourali, A. R.; Cheraghi-Parvin, M.; Omidi-Ghallemohamadi, M. Synthesis of Cu (II) Schiff base complex supported on multi-wall carbon nanotube for the oxidation of benzyl alcohols. *Inorg. Chem. Commun.* **2023**, *155*, 111099.

(52) Hong, P. D.; Zhang, K. S.; He, J. Y.; Li, Y. L.; Wu, Z. J.; Xie, C.; Liu, J. H.; Kong, L. T. Selenization governs the intrinsic activity of copper-cobalt complexes for enhanced non-radical Fenton-like oxidation toward organic contaminants. *J. Hazard. Mater.* **2022**, *435*, 128958.

(53) Zhou, S.; Liao, W.; Wang, Z.; Pan, H.; Liu, F.; Lin, Q.; Wang, Q. Structurally ordered PtFe intermetallic embedded in N-doped carbon as a highly active and durable electrocatalyst for oxygen reduction reaction. *Int. J. Hydrogen Energy* **2022**, *47* (2), 1256−1266.

(54) Ahn, H. J.; Lee, J. S.; Kim, H. S.; Hwang, I. T.; Hong, J. H.; Shin, J.; Jung, C. H. Fabrication of large Pt nanoparticles-decorated rGO counter electrode for highly efficient DSSCs. *J. Ind. Eng. Chem.* **2018**, *65*, 318−324.

(55) Ren, G. H.; Zhang, Z. C.; Liu, Y. J.; Liang, Y.; Zhang, X. C.; Wu, S. S.; Shen, J. One-pot solvothermal preparation of ternary PdPtNi nanostructures with spiny surface and enhanced electrocatalytic performance during ethanol oxidation. *J. Alloys Compd.* **2020**, *830*, 154671.

(56) Huang, W.; Kang, X.; Xu, C.; Zhou, J.; Deng, J.; Li, Y.; Cheng, S. 2D PdAg Alloy Nanodendrites for Enhanced Ethanol Electroxidation. *Adv. Mater.* **2018**, *30* (11), 1706962.

(57) Tan, J. L.; De Jesus, A. M.; Chua, S. L.; Sanetuntikul, J.; Shanmugam, S.; Tongol, B. J. V.; Kim, H. Preparation and characterization of palladium-nickel on graphene oxide support as anode catalyst for alkaline direct ethanol fuel cell. *Appl. Catal. A-Gen.* **2017**, *531*, 29−35.

(58) Chowdhury, S. R.; Maiyalagan, T. Enhanced Electro-catalytic Activity of Nitrogen-doped Reduced Graphene Oxide Supported PdCu Nanoparticles for Formic Acid Electro-oxidation. *Int. J. Hydrogen Energy* **2019**, *44* (29), 14808−14819.

(59) Duan, J. J.; Feng, J. J.; Zhang, L.; Yuan, J. H.; Zhang, Q. L.; Wang, A. J. Facile one-pot aqueous fabrication of interconnected ultrathin PtPbPd nanowires as advanced electrocatalysts for ethanol oxidation and oxygen reduction reactions. *Int. J. Hydrogen Energy* **2019**, *44* (50), 27455−27464.

(60) Yang, Y.; Huang, H. J.; Shen, B. F.; Jin, L.; Jiang, Q. G.; Yang, L.; He, H. Y. Anchoring nanosized Pd on three-dimensional boron- and nitrogen-codoped graphene aerogels as a highly active multifunctional electrocatalyst for formic acid and methanol oxidation reactions. *Inorg. Chem. Front.* **2020**, *7* (3), 700−708.

(61) Wu, T.; Ma, Y.; Qu, Z. B.; Fan, J. C.; Li, Q. X.; Shi, P. H.; Xu, Q. J.; Min, Y. L. Black Phosphorus-Graphene Heterostructure-Supported Pd Nanoparticles with Superior Activity and Stability for Ethanol Electro-oxidation. *ACS Appl. Mater. Interfaces* **2019**, *11* (5), 5136−5145.

(62) Zheng, Y. Y.; Qiao, J. H.; Yuan, J. H.; Shen, J. F.; Wang, A. J.; Huang, S. T. Controllable synthesis of PtPd nanocubes on graphene as advanced catalysts for ethanol oxidation. *Int. J. Hydrogen Energy* **2018**, *43* (10), 4902−4911.

(63) Luo, L. X.; Fu, C. H.; Yang, F.; Li, X. L.; Jiang, F. L.; Guo, Y. G.; Zhu, F. J.; Yang, L. J.; Shen, S. Y.; Zhang, J. L. Composition-Graded Cu-Pd Nanospheres with Ir-Doped Surfaces on N-Doped Porous Graphene for Highly Efficient Ethanol Electro-Oxidation in Alkaline Media. *ACS Catal.* **2020**, *10* (2), 1171−1184.

(64) Wang, Y.; Zheng, M.; Li, Y.; Ye, C.; Chen, J.; Ye, J.; Zhang, Q.; Li, J.; Zhou, Z.; Fu, X.-Z.; et al. p−d Orbital Hybridization Induced by a Monodispersed Ga Site on a Pt_3Mn Nanocatalyst Boosts Ethanol Electrooxidation. *Angew. Chem., Int. Ed.* **2022**, *61* (12), No. e202115735.